Interactions between a Submesoscale Anticyclonic Vortex and a Front*

CÉDRIC CHAVANNE AND PIERRE FLAMENT

School of Ocean and Earth Science and Technology, University of Hawaii at Manoa, Honolulu, Hawaii

KLAUS-WERNER GURGEL

Institute of Oceanography, University of Hamburg, Hamburg, Germany

(Manuscript received 13 May 2008, in final form 5 March 2010)

ABSTRACT

The evolution of a submesoscale anticyclonic vortex was observed by high-frequency Doppler radio current meters and satellite radiometers. The vortex formed between two large cyclones to the southwest of Oahu, Hawaii. The radius of the core was ~15 km; the azimuthal velocity reached 35 cm s^{-1}; and the surface vorticity remained below $-f$ for 9 days, reaching an extremum of $-1.7f$. The flow was ageostrophic near the center and around the periphery of the vortex. The initial growth may have been driven by negative wind stress curl in the lee of Oahu. The vortex was prone to inertial, symmetric, and anticyclonic ageostrophic instabilities, but the temporal evolution of radial profiles of vorticity was inconsistent with angular momentum redistribution by inertial instability.

A tongue of surface water 0.7°C warmer became entrained northward between the vortex and the colder cyclone to the west. As the vortex strengthened, a 0.14°C km^{-1} front formed along the eastern flank of the tongue. The sea surface temperature gradient remained weaker on the western flank. The flow was anticyclonic ($-0.4f$) and divergent ($0.1f$) on the warm side of the front but cyclonic ($0.6f$) and convergent ($-0.2f$) on the cold side. This suggests ageostrophic cross-frontal circulations maintaining alongfront thermal wind balance in the presence of large-scale strain $\overline{\sigma}$. Surface divergence δ was proportional to vorticity ζ during the 3-day frontogenesis: $\delta \sim -(\overline{\sigma}/f)\zeta$. This is consistent with a semigeostrophic model of a front confined to a surface layer of zero potential vorticity.

1. Introduction

Mesoscale and submesoscale eddies dominate upper ocean variability. They affect the meridional, zonal, and cross-thermocline transport of properties, upper stratification, as well as primary productivity. Resolving submesoscale structures in observations and parameterizing them in numerical models is challenging.

The Hawaiian archipelago is a prime region for studying such processes. The Hawaiian Ridge presents a barrier to the North Equatorial Current, and ocean eddies are generated by wake instability (Patzert 1969; Lumpkin 1998; Flament et al. 2001). The islands present barriers to the trade winds, and ocean eddies are generated by Ekman pumping from the atmospheric wakes (Patzert 1969; Lumpkin 1998; Chavanne et al. 2002). Finally, the subtropical front system (Roden 1981) sometimes extends southward to the latitude of Hawaii, forming eddies by frontal instabilities (Hosegood et al. 2008, Fig. 1).

The eddy field for the last week of October 2002 is shown in Fig. 1. Sea surface temperature (SST) images (Figs. 1a,c) reveal three cyclones: L_1 centered at (21.3°N, 159.4°W) south of Kauai, L_2 centered at (20.7°N, 158.1°W) south of Oahu, and L_3 centered at (20.1°N, 156.9°W) south of Maui. Their cold cores resulted from advection of cold water from northeast of the ridge, augmented by local upwelling (the L_3 core was colder than any surrounding water). Indeed, the cyclones initially appeared under strong positive wind stress curl anomalies in the lee of Hawaii and Maui (Fig. 1d) before drifting westward or northward. Surface currents inferred from gridded satellite altimetry are too coarse to fully resolve

* University of Hawaii at Manoa School of Ocean and Earth Science and Technology Contribution Number 7759.

Corresponding author address: Cédric Chavanne, School of Environmental Sciences, University of East Anglia, Norwich NR4 7TJ, United Kingdom.
E-mail: cedric.chavanne@ensta.org

DOI: 10.1175/2010JPO4055.1

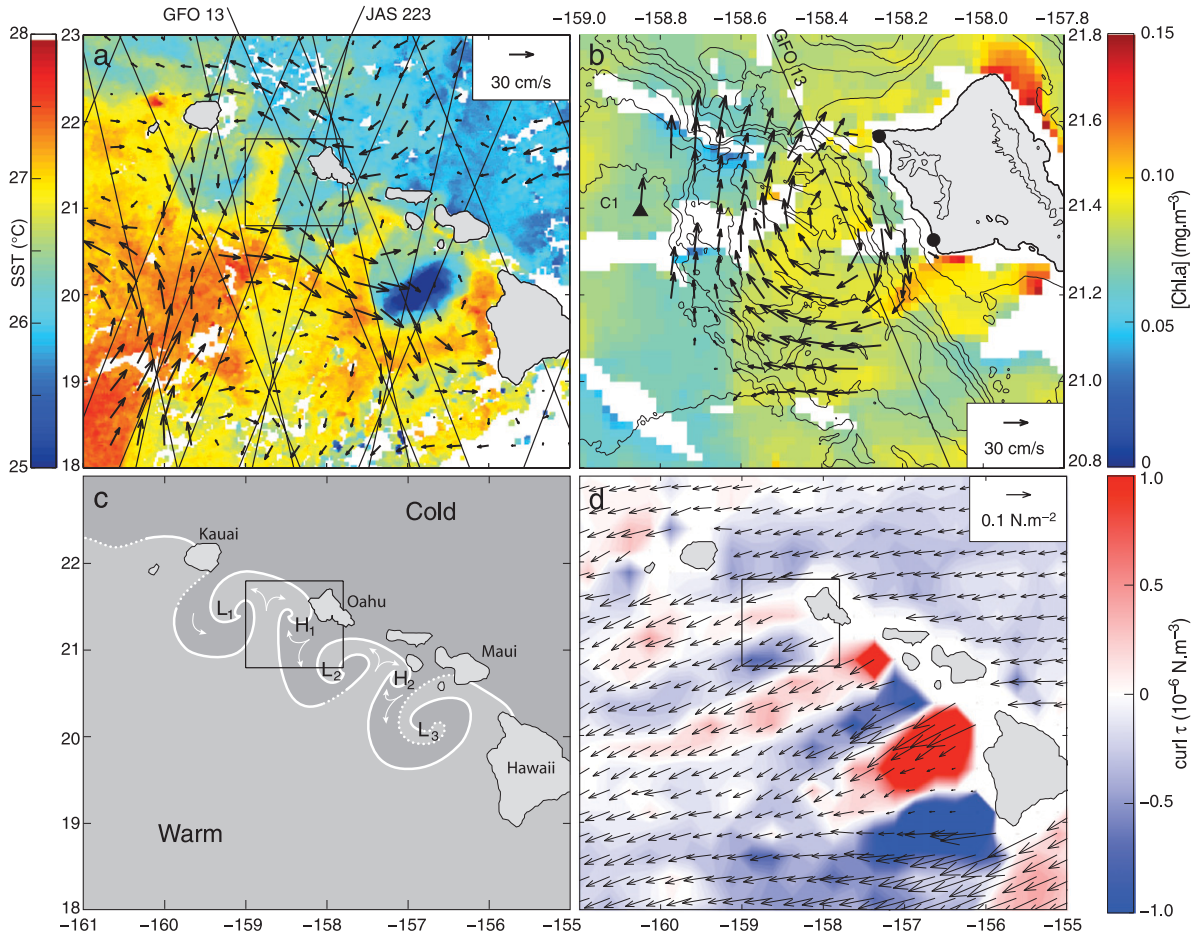

FIG. 1. (a) Altimetric surface geostrophic currents for 23–30 Oct 2002, overlaid on a composite SST image from *Aqua* and *Terra* MODIS for 26 Oct. The tracks of the *Jason-1*, *European Remote Sensing Satellite-2* (*ERS-2*), *GFO*, and Ocean Topography Experiment (TOPEX)/Poseidon altimeters are shown as black lines. (b) Subinertial surface currents for 27 Oct from HFRs (marked by black bullets) and from ADCP C1 (12-m-depth bin, marked by a black triangle), overlaid on chlorophyll-*a* concentration from *Aqua* MODIS at 2355 UTC 26 Oct. Bathymetry is contoured every 500 m. (c) Conceptual sketch of the main SST and circulation features (H: anticyclones, L: cyclones). (d) Wind stress and curl from QuikSCAT at 25-km resolution, averaged over 23–30 Oct. The coverage of (b) is outlined in (a),(c), and (d).

these cyclones, although they are well sampled along track (the gridding filter has a 200-km cutoff scale, Ducet et al. 2000).

Observations by high-frequency Doppler radio (HFR) current meters, with a resolution of 2 km, overcome the limited resolution of altimetry and reveal energetic submesoscale vortices embedded in the larger-scale eddy field, such as the 15-km radius anticyclonic vortex H_1 seen southwest of Oahu in Fig. 1b. Vortex pairs such as L_1 and H_1 advected SST into the hammerhead patterns sketched in Fig. 1c. The warm SST tongue entrained between these vortices was asymmetric, with a sharper front on the eastern side.

In this paper, we describe the structure and dynamics of this energetic submesoscale anticyclonic vortex and the associated frontogenesis. We will show that (i) the absolute vorticity (planetary plus relative) was negative for 9 days in the core of the vortex, making it susceptible to inertial, symmetric, and anticyclonic ageostrophic instabilities; (ii) the flow was ageostrophic near the center and around the periphery of the vortex; (iii) straining of the SST field by the vortex and by cyclone L_1 triggered frontogenesis and ageostrophic cross-frontal circulations; and (iv) divergence along the front was proportional to the local vorticity of the jet, conforming to the semigeostrophic model of a front confined to a surface layer of zero potential vorticity (Hoskins and Bretherton 1972).

The methods used to separate subinertial submesoscale processes from near-inertial oscillations and internal tides are presented in section 2. The subinertial observations are described in section 3. The dynamics of the vortex and of the SST front are discussed in sections 4 and 5. The results and broader implications are summarized

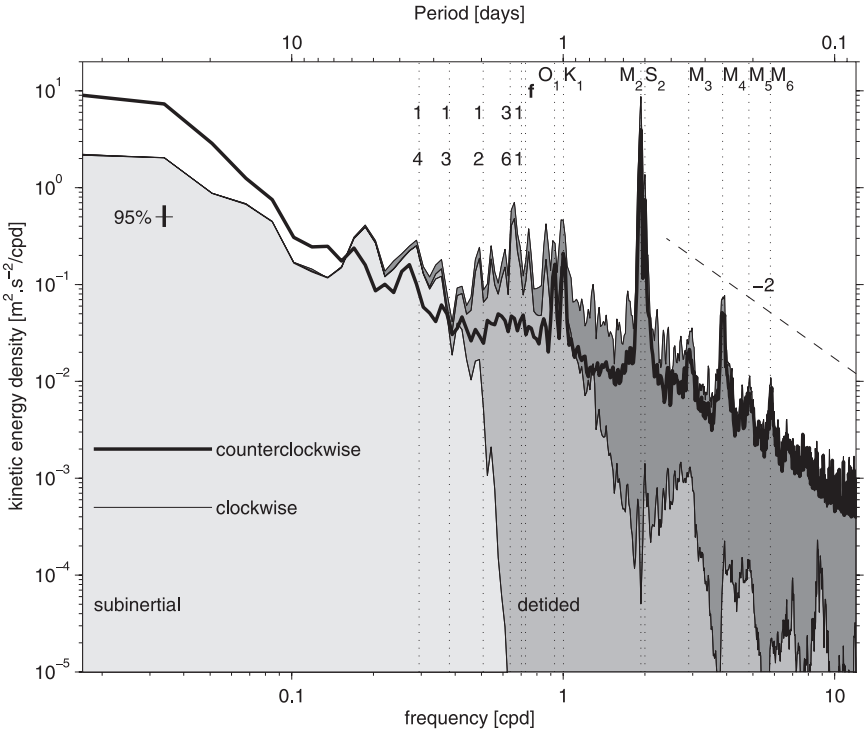

FIG. 2. Rotary power spectra for 11 Sep–9 Nov 2002, spatially averaged over grid points with more than 90% data return, covering 66% of the observed area. Clockwise and counterclockwise components are plotted with thin and thick lines, respectively. The successive temporal filters (hourly observed, detided, and subinertial) are shown with increasingly lighter shadings. Vertical dotted lines indicate the major tidal constituents, the inertial frequency f, and island-trapped modes, with the upper and lower digits referring to the azimuthal and vertical mode numbers. The slanted dashed line shows the −2 spectral slope. The 95% confidence interval assumes one independent degree of freedom per 3 × 3 grid cell.

and discussed in section 6. The instruments, datasets, and processing are detailed in the appendix.

2. Methods

Two HFR current meters were deployed along the west shore of Oahu (Fig. 1b) from September 2002 to May 2003. Each HFR current meter measured the radial component of surface currents. Radial currents were averaged hourly and mapped into vector currents on a 2-km resolution Cartesian grid, as described in the appendix.

Figure 2 shows the spatially averaged rotary spectra during fall 2002. At high frequencies, the continuum energy falls off with a −2 slope characterizing the Garrett–Munk spectrum, with no rotary asymmetry. The semidiurnal tides dominate the superinertial bands. The diurnal tides are a factor of 10 weaker. In contrast, clockwise energy is larger than counterclockwise in a broad near-inertial band. The strongest near-inertial peak occurs at $\sim 0.9f$. Since the inertial frequency is shifted to $f + \zeta/2$ in the presence of local vorticity ζ (Kunze 1985), this suggests that $\zeta \sim -0.2f$, similar to the observed vorticity averaged over two months (not shown). Peaks at lower frequencies between f and 7 days are possibly associated with island-trapped waves (Luther 1985; Merrifield et al. 2002), which may also contribute to the peak at $\sim 0.9f$. For periods longer than 7 days, counterclockwise energy dominates.

Figure 3 shows the spatially averaged spectra of vorticity $\zeta = \partial v/\partial x - \partial u/\partial y$ and divergence $\delta = \partial u/\partial x + \partial v/\partial y$. Tidal peaks are strong, because internal tides generated over topography vary over small spatial scales, and their amplitudes and phases are modulated by mesoscale currents (Chavanne et al. 2010a,b), enhancing spatial gradients. There are no distinct near-inertial peaks in the spectra of vorticity and divergence.

Submesoscale flows due to surface density anomalies can reach a Rossby number $\mathrm{Ro} = |\zeta/f|$ of order one (Blumen 1978; Held et al. 1995) and, thus, may have advective time scales similar to the inertial period (33 h at this latitude). They are dynamically distinct, however,

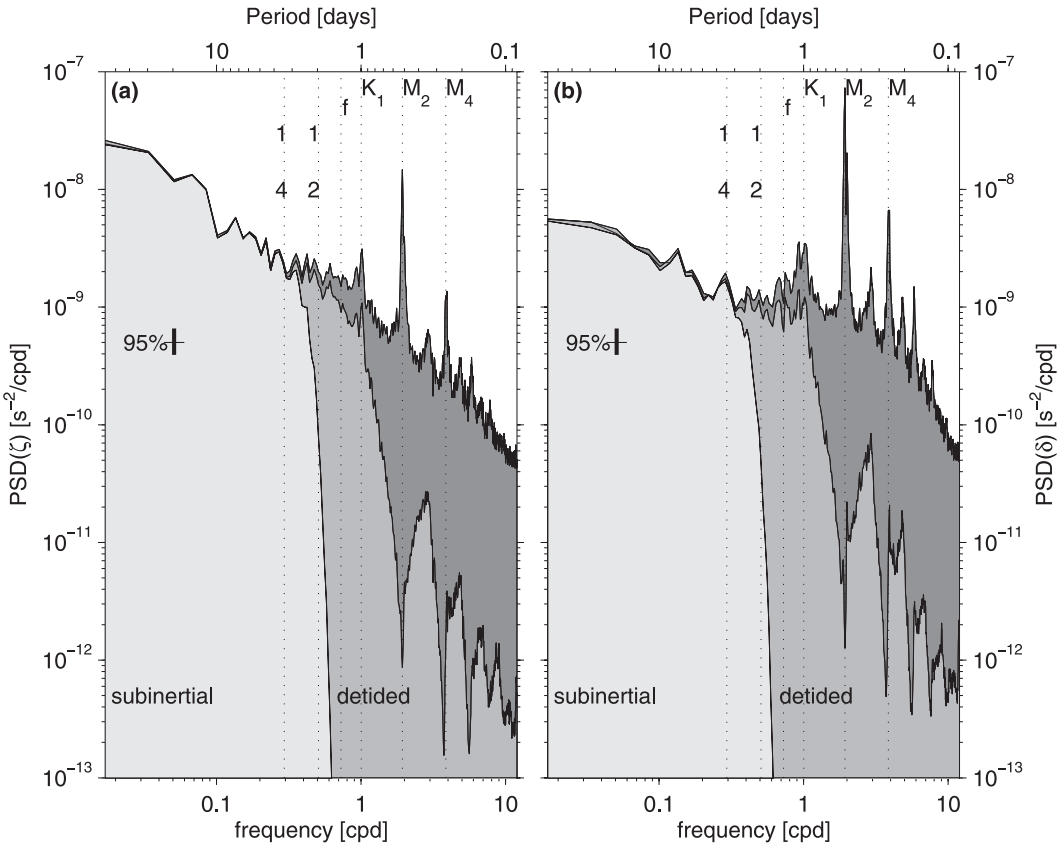

FIG. 3. As in Fig. 2, but for (a) vorticity and (b) divergence.

from near-inertial oscillations. Near-inertial oscillations and tides must thus be cautiously filtered out to isolate submesoscale processes.

The strong semidiurnal M_2 tide was first removed by successive least squares fits (amplitude, phase, and mean) over a 2-day sliding window to reduce spectral leakage into lower frequencies. Small data gaps were then linearly interpolated, and the residual currents were subject to a 12-h moving average to obtain the time series of detided currents in which semidiurnal vorticity and divergence have, in effect, been removed (Fig. 3). Nonlinear terms in the equations of momentum, divergence, and vorticity were computed from these detided currents to retain correlations on near-inertial time scales.

All quantities (velocity, vorticity, divergence, and nonlinear terms) were individually low-pass filtered by a 44-step finite impulse response filter, run forward and backward, with a 2-day cutoff period. Subinertial vorticity and divergence are not affected by this filter (Fig. 3). Computing the nonlinear terms directly from the low-pass filtered currents, instead of the detided currents, yields indistinguishable results. This paper focuses on subinertial currents, from which tides and near-inertial oscillations have been filtered out. The uncertainties of the subinertial quantities are estimated as the standard deviation of the detided quantities over one inertial period.

The anticyclone characteristics (center, radius, etc.) were determined as follows. For each subinertial current snapshot, the spatial average over the HFR domain was removed to separate the vortex from the background currents. The vortex center was defined as the location of the minimum residual velocity inside the anticyclonic circulation. Currents were bilinearly interpolated onto a polar grid with the origin at the vortex center and projected on the radial and azimuthal directions. The azimuthal velocity component was azimuthally averaged to obtain the radial profile of vortex velocity V. The vortex radius R_m was defined as the distance from the center r where the vortex velocity reached a local extremum value, V_m. Finally, the extremum vorticity ζ_m inside the vortex core ($r \leq R_m$) was determined.

3. Description of observations

Figure 4 shows subinertial surface currents and SST composites at different stages of the evolution of the anticyclonic vortex, Fig. 5 shows time series of vortex

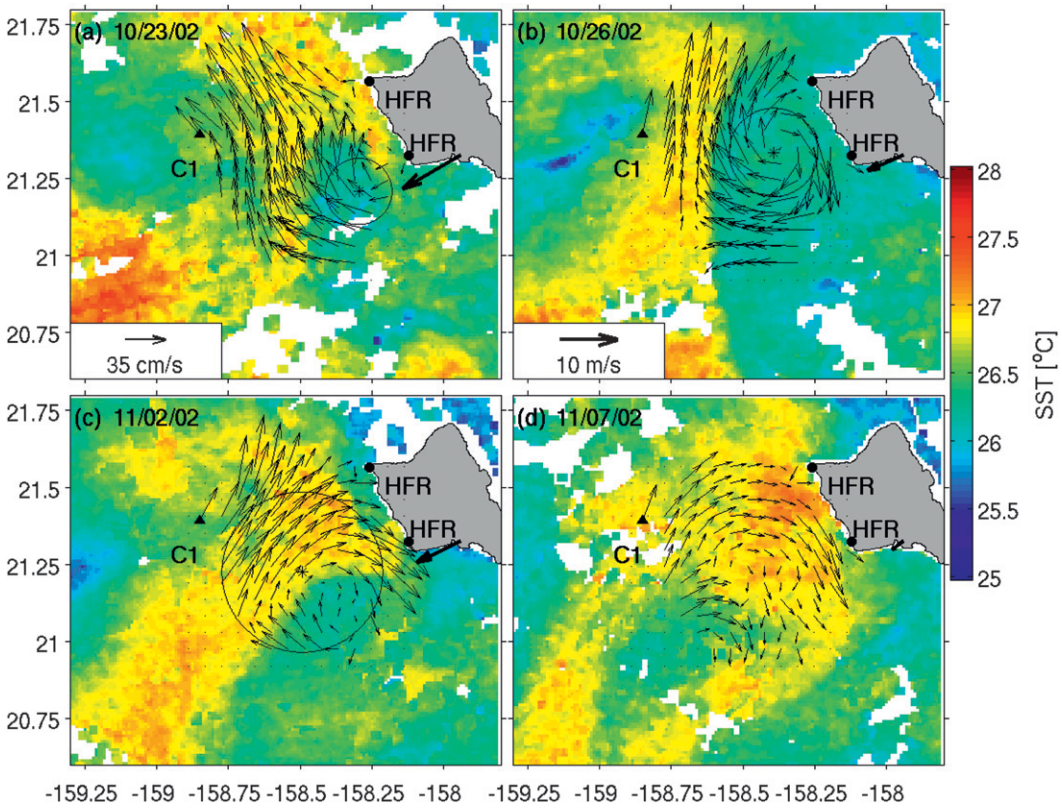

FIG. 4. Low-pass-filtered currents from HFRs and ADCP C1 (thin arrows) and 10-m wind at Honolulu International Airport (thick arrows), overlaid on daily composite SSTs from *Aqua* and *Terra* MODIS, for (a) 23 Oct, (b) 26 Oct, (c) 2 Nov, and (d) 7 Nov 2002. The vortex center positions are indicated by black stars, and its core boundaries by black circles, except in (d).

characteristics (R_m, V_m, and ζ_m), and Fig. 6 shows radial profiles of V and absolute vorticity, $f + \zeta$.

On 20 October, prior to the genesis of the anticyclonic vortex, cyclones L_1 and L_2 were lying west and south of Oahu, as suggested by cooler SST near (21.2°N, 159.0°W) and (21.0°N, 157.9°W). The northward flow between L_1 and the coast was sheared anticyclonically, with vorticity reaching $-0.8f$.

The anticyclonic vortex first appeared as a closed circulation in the residual current field on 23 October but was not yet discernible in the total current field because it was embedded in a stronger and larger meander around the southwest point of Oahu (Fig. 4a). It had a radius of 10 km, maximum azimuthal velocity of 13 cm s^{-1}, and extremum vorticity $\zeta_m = -f$ (Figs. 5a,b). A tongue of surface water 0.7°C warmer became entrained northward between the vortex and the colder cyclone L_1.

On 26 October (Fig. 4b), the vortex was fully developed with a radius of ~15 km and maximum azimuthal velocity of 35 cm s^{-1}, reaching a vorticity of $-1.7 \pm 0.1f$ (Figs. 5a,b). The absolute vorticity $f + \zeta$ was negative within ~8 km of the vortex center (Fig. 6b), making it prone to inertial instability (section 4b). The vorticity structure is detailed in Fig. 7a. The anticyclonic core was surrounded by a narrow (~8 km) cyclonic rim to the west and south and along the coast to the east.

As the vortex strengthened, a front formed along the eastern flank of the warm tongue; the SST gradient reached a maximum of 0.14°C km^{-1} at 158.62°W. In contrast, the SST gradient remained five times weaker on the western flank (Fig. 8a). The southward thermal wind balancing the SST front is visible as a local weakening of the northward flow (Fig. 8b). The flow was anticyclonic ($-0.45 \pm 0.03f$) and divergent ($0.11 \pm 0.05f$) over 14 km on the warm side of the front but cyclonic ($0.58 \pm 0.14f$) and convergent ($-0.17 \pm 0.05f$) over 10 km on the cold side (Fig. 8c; here only, ± are standard deviations over the averaging interval 21.1°–21.3°N).

By 2 November (Fig. 4c), the vortex had broadened and weakened, with a radius of ~30 km and maximum azimuthal velocity of 25 cm s^{-1} (Fig. 5a). The sudden radius increase on 1 November is reminiscent of the vortex pairing events observed by Flament et al. (2001) in the lee of the island of Hawaii. The vortex had become

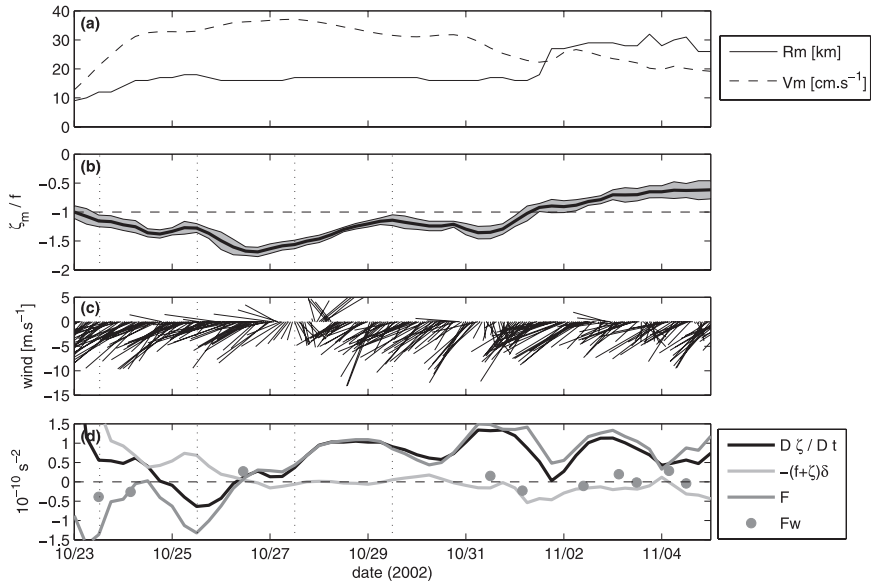

FIG. 5. Time series of (a) vortex radius (solid line) and maximum azimuthally averaged azimuthal velocity component (dashed line), (b) extremum vorticity within the vortex core (solid line; shading represents uncertainty), (c) hourly 10-m wind at Honolulu International Airport, and (d) vorticity balance terms [Eq. (3)] averaged over the vortex core. The horizontal dashed line in (b) marks the inertial instability threshold ($\zeta = -f$). The gray bullets in (d) represent vorticity forcing by wind stress curl [Eq. (4)] from QuikSCAT observations averaged over the vortex core.

inertially stable ($\zeta_m = -0.9f$), but small vortices developed inside the core. The SST front on the eastern flank of the warm tongue had weakened and rotated anticyclonically, advected around the vortex. Simultaneously, advection of the warm tongue around cyclone L_1 resulted in the hammerhead SST pattern sketched in Fig. 1c.

On 7 November (Fig. 4d), the vortex had split into two embedded vortices, and a patch of colder water became entrapped as the warm SST tongue completed its loop around the anticyclonic core. These snapshots illustrate transfers of energy to both larger and smaller scales: the anticyclonic vortex grew with time, while fronts developed and smaller vortices formed.

The vertical structure of currents was measured at mooring C1 (Fig. 1b), which unfortunately was outside the anticyclonic vortex. Figure 9a shows the first empirical orthogonal function (EOF) of currents as a function of depth. Currents were surface intensified and decayed exponentially with depth with a scale $H \sim 100$ m, faster than the first baroclinic mode computed from nearby hydrographic observations (Fig. 9b). Variability at C1 was dominated by eddies, such as L_1, with diameters ~ 60 km. The vertical scales of smaller features, such as the anticyclonic vortex ($\sim$30 km) and the SST front ($\sim$12 km), can be expected to be smaller than 100 m (Lapeyre and Klein 2006a).

4. Dynamics of the anticyclonic vortex

a. Momentum balance

Balanced vortices with finite Rossby number, such as the anticyclone described in section 3 [$\partial\delta/\partial t$ is an order

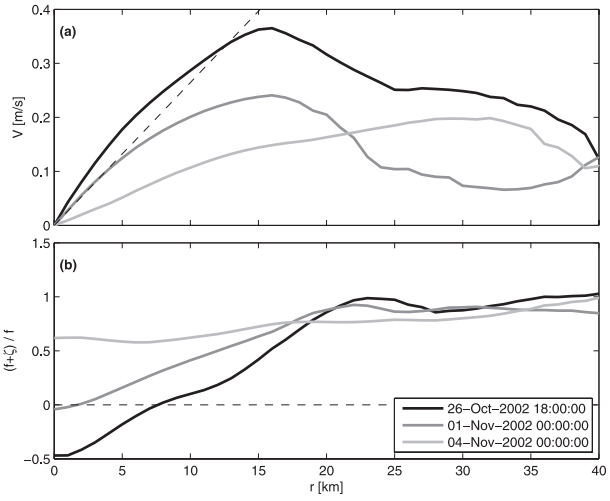

FIG. 6. Radial profiles of azimuthally averaged (a) azimuthal velocity component and (b) absolute vorticity, $f + \zeta$, normalized by f on 26 Oct (black lines), 1 Nov (dark gray lines), and 4 Nov (light gray lines). The dashed line in (a) represents the velocity profile of a marginally stable anticyclonic vortex, $V = fr/2$, for which the absolute vorticity is zero [dashed line in (b)].

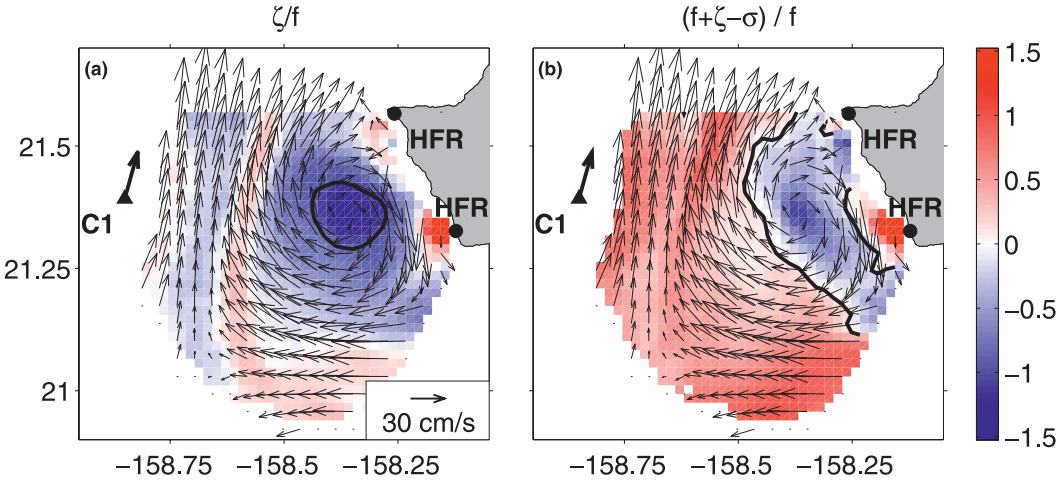

FIG. 7. Instability criteria at extremum of vorticity on 26 Oct 2002: (a) relative vertical vorticity ζ, normalized by f, with the inertial instability criterion $\zeta/f < -1$ shown by a black contour and (b) absolute vorticity $f + \zeta$ minus strain σ, normalized by f, with the ageostrophic anticyclonic instability criterion $f + \zeta - \sigma < 0$ shown by a black contour.

of magnitude weaker than the terms in Eq. (1)], verify the gradient wind balance, where Coriolis and advective accelerations balance the pressure force, obtained from the divergence of the momentum equation:

$$g\nabla^2 h = -\nabla \cdot (\mathbf{u} \cdot \nabla u) + f\zeta, \tag{1}$$

where $\mathbf{u}$ and ζ are the surface subinertial currents and vorticity, h the sea level anomaly (SLA), and hydrostatic balance has been assumed. When $\nabla \cdot (\mathbf{u} \cdot \nabla \mathbf{u})$ is small, Eq. (1) yields geostrophic balance. The degree of ageostrophy ϵ is given by

$$\epsilon = \frac{|f\zeta - g\nabla^2 h|}{|f\zeta| + |g\nabla^2 h|}, \tag{2}$$

where the SLA Laplacian is estimated from the observed currents using Eq. (1). When $\epsilon \ll 1$, the flow is in

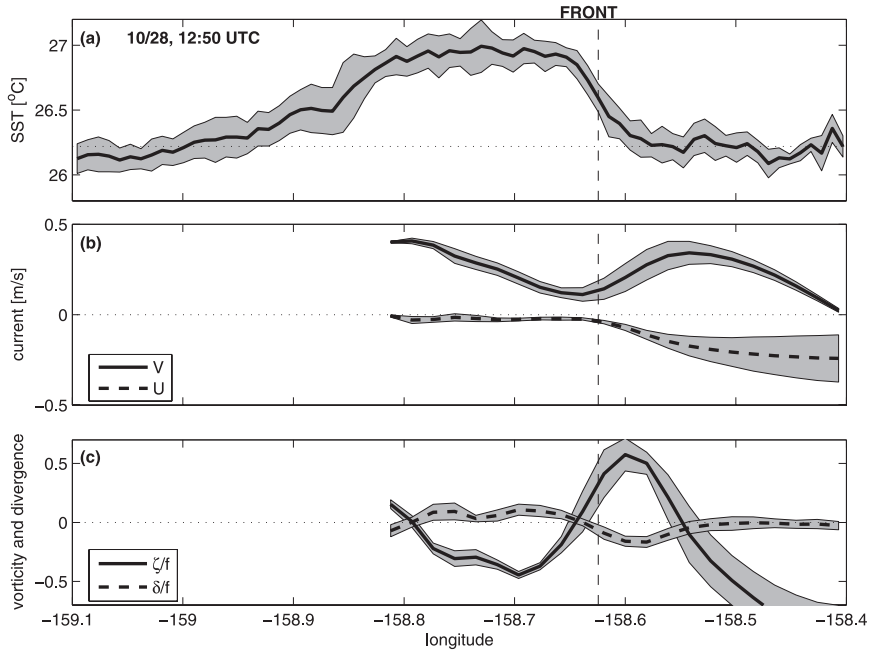

FIG. 8. Zonal sections, averaged over (21.1°–21.3°N) where the front was meridional, of (a) SST from *Aqua* MODIS at 1250 UTC 28 Oct; (b) zonal (dashed) and meridional (solid) currents from HFRs; and (c) vorticity (solid) and divergence (dashed), normalized by f. Shadings indicate standard deviations over (21.1°–21.3°N).

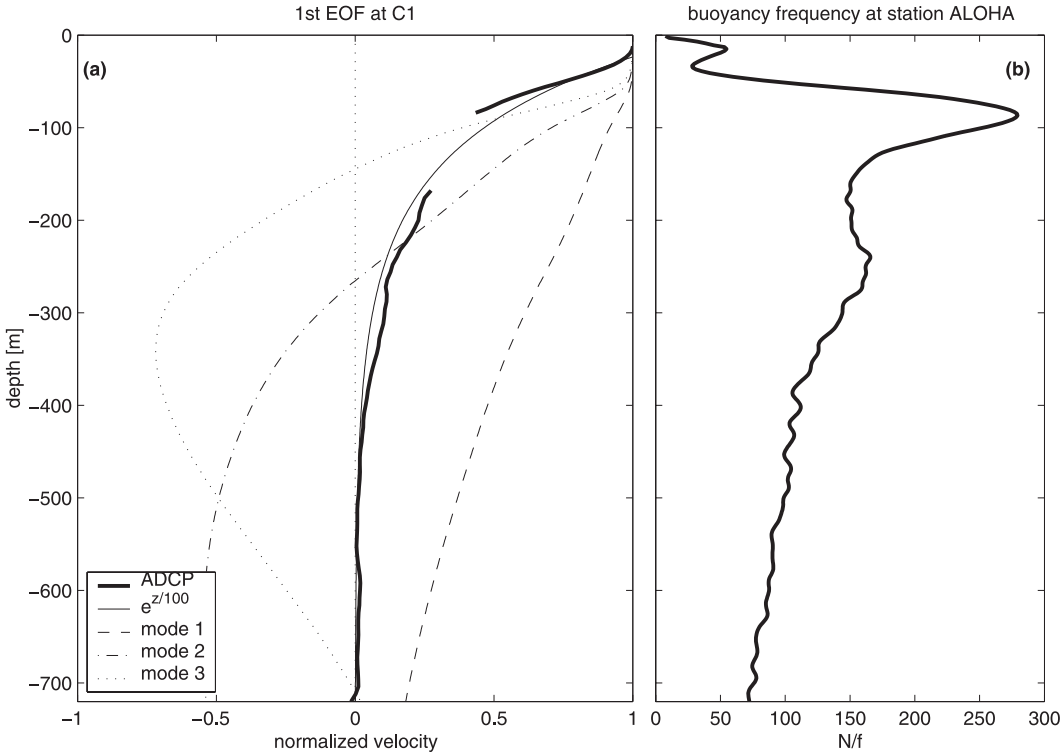

FIG. 9. (a) First EOF of currents as a function of depth at mooring C1 (thick line), computed over the period from 14 Sep to 8 Nov 2002. This EOF explains 88% of the variance. An exponential fit (thin line) and the first three vertical normal modes computed from the buoyancy frequency profile (dashed, dot-dashed, and dotted lines) are shown. (b) Buoyancy frequency profile 100 km north of Oahu, from hydrographic observations to 4700-m depth in Sep–Nov 2002 (Fujieki et al. 2005).

approximate geostrophic balance. In Fig. 10, ϵ is shown for 27 October when vorticity reached an extremum. Owing to the large Rossby number (Ro = 1.7), the flow was ageostrophic, especially near the center and around the periphery of the vortex, where $\epsilon > 0.5$. A comparable degree of ageostrophy was found in numerical experiments by Capet et al. (2008b).

A different attempt to assess the momentum balance of the vortex was made by comparing sea level anomalies, measured along track by satellite altimeters [*Geosat Follow-On* (*GFO*) and *Jason-1*], with sea level anomalies computed by along-track integration of the momentum equations, using the currents observed by the HFRs. This comparison was inconclusive because sea level anomalies were dominated by internal tides, known to be energetic in this area (Chavanne et al. 2010a), and the residual signals after their removal were too noisy to detect the submesoscale vortex.

b. Vorticity balance

To investigate the mechanisms responsible for the growth and decay of the vortex, the subinertial surface vorticity balance was estimated:

$$D\zeta/Dt = -(f + \zeta)\delta + F, \tag{3}$$

where $D\zeta/Dt = \partial\zeta/\partial t + \mathbf{u} \cdot \nabla\zeta$ is the Lagrangian rate of change of vorticity, caused by vortex stretching $[-(f + \zeta)\delta]$

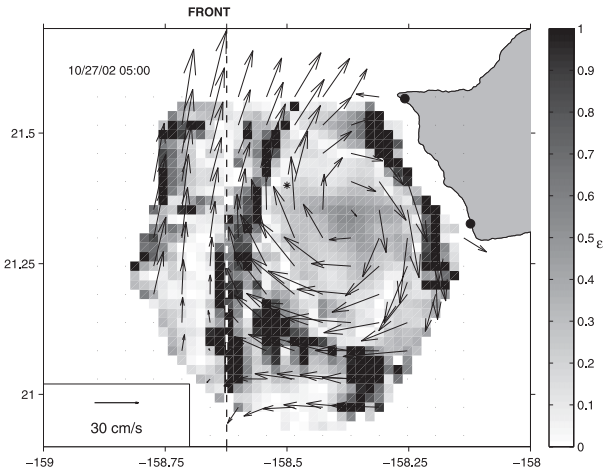

FIG. 10. Degree of ageostrophy ϵ from Eq. (2) on 27 Oct 2002. The location of the SST front is shown by a dashed line, with increased thickness between 21.1° and 21.3°N.

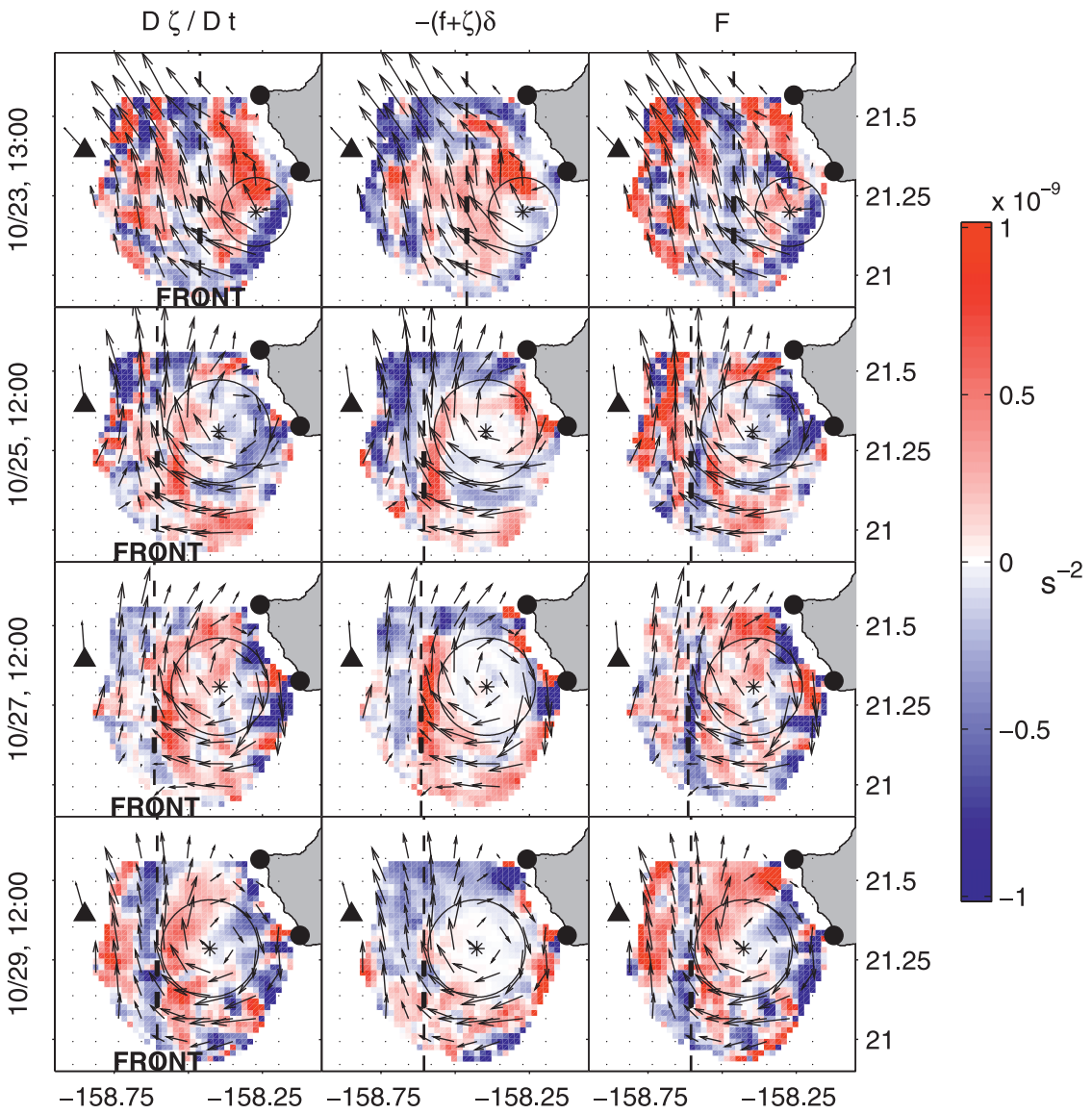

FIG. 11. Snapshots of the terms of the surface vorticity balance [Eq. (3)], with surface currents overlaid. (left) to (right) Lagrangian rate of change of vorticity, vortex stretching, and friction plus noise. The times of the snapshots are at 1300 UTC 23 Oct, 1200 UTC 25 Oct, 1200 UTC 27 Oct, and 1200 UTC 29 Oct. The location of the SST front is shown by a dashed line, with increased thickness between 21.1° and 21.3°N. The vortex center positions are indicated by black stars, and its core boundaries by black circles.

and friction F computed as a residual, therefore containing measurement noise. Figure 11 shows the spatial distribution on four different days of each term of the vorticity balance, and Fig. 5d shows time series of their net effect averaged over the vortex core. The evolution of vorticity within the vortex core was dominated by frictional processes, which drove the strengthening of anticyclonic vorticity prior to 27 October and its weakening afterward. The spatial averaging prior to 25 October is misleading because of the inclusion of a strong positive vortex stretching patch associated with a SST front parallel to the coast ~10 km offshore (see Fig. 12, top, and section 5). It drove a strong increase of vorticity in the northern part of the vortex core (Fig. 11a), which dominated the vorticity decrease in the southeastern half of the core where the vorticity extremum was strengthening (Fig. 5b).

Could frictional forcing be wind induced? The contribution of wind stress τ to F can be scaled as

$$F_w = \frac{1}{\rho H_E}\mathrm{curl}_z\tau, \qquad (4)$$

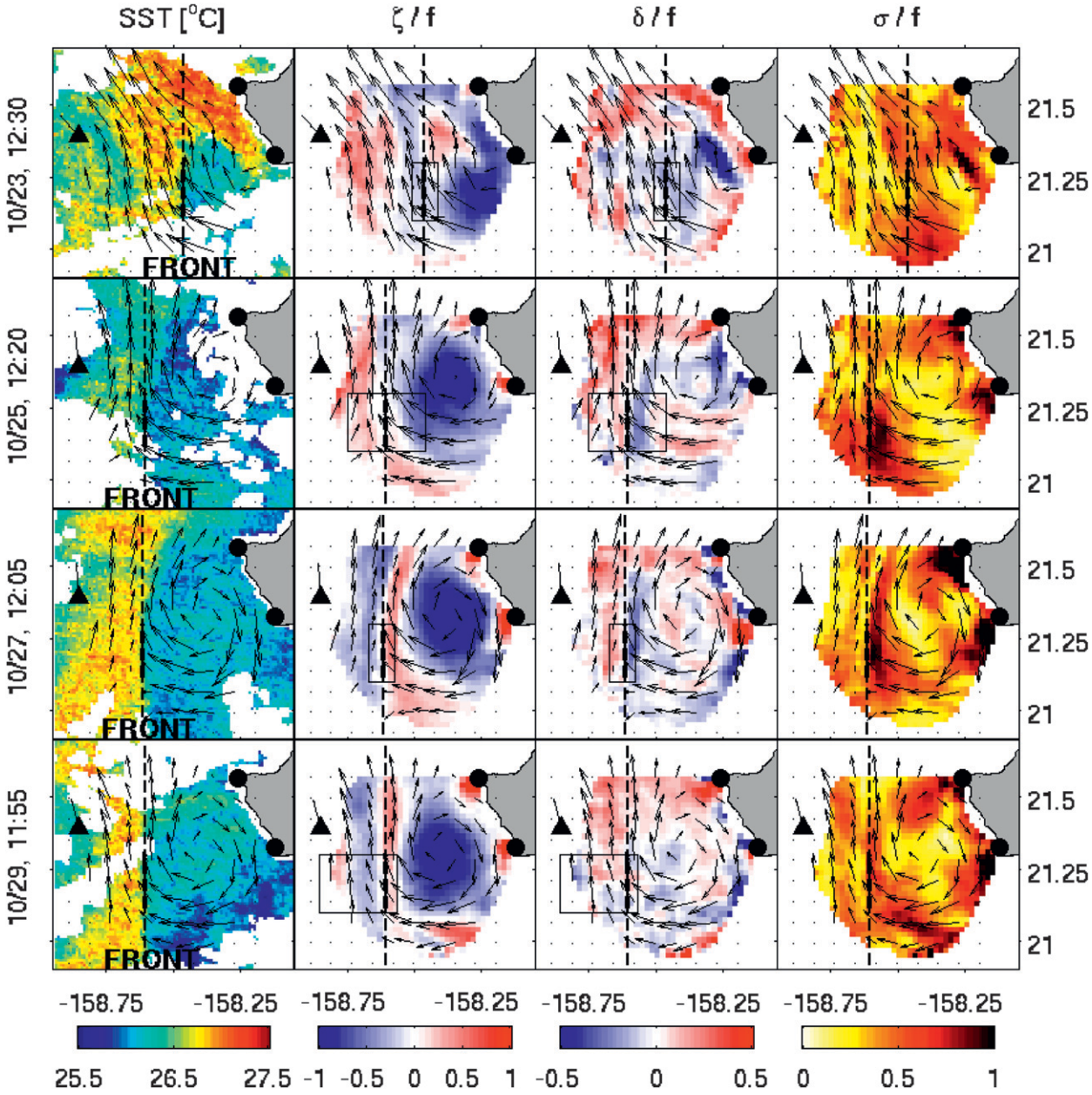

FIG. 12. (left) to (right) Evolution of SST, vorticity, divergence, and strain rate, with the surface currents overlaid. The times of the snapshots are at 1230 UTC 23 Oct, 1220 UTC 25 Oct, 1205 UTC 27 Oct, and 1155 UTC 29 Oct. The location of the SST front is shown by a dashed line, with increased thickness between 21.1° and 21.3°N. The black boxes in the vorticity and divergence panels indicate some of the areas over which the quantities shown in Fig. 14 were estimated.

where $\rho = 1025$ kg m^{-3} is the density of seawater, $H_E =$ 20 m is the Ekman layer depth, and $\mathrm{curl}_z\tau$ is the wind stress curl. The latter was computed from Quick Scatterometer (QuikSCAT) ascending and descending tracks, bilinearly interpolated on the HFR grid, and averaged over the vortex core. In Fig. 5d, F_w is shown by gray bullets. QuikSCAT observations over the anticyclone core were sporadic, but prior to 27 October, however, the few F_w values available compare well with the F values estimated from the HFR observations, suggesting that wind stress curl could have driven the anticyclonic vorticity growth. The wind direction became more variable at the end of 26 October (Fig. 5c), and wind stress curl changed sign at the time when the anticyclone vorticity peaked. However, the subsequent vorticity decay was driven by frictional forcing stronger

than that contributed by the wind, at least after 31 October.

Could the vorticity decay after 27 October have been driven by unresolved processes, such as inertial, symmetric, and ageostrophic anticyclonic instabilities, which may act when the anticyclonic vorticity is large? For barotropic flows, the inertial instability criterion is (e.g., Holton 1992, p. 207)

$$f(f+\zeta)<0. \tag{5}$$

Inertial instability redistributes angular momentum radially until the vortex becomes inertially stable. The criterion was verified within 8 km from the center (where $f+\zeta<0$) on 26 October (Fig. 6b). Restabilization occurred after 1 November, when $f+\zeta>0$ everywhere. However, if inertial instability was responsible for increasing the absolute vorticity above zero near the vortex center, it should have simultaneously decreased the absolute vorticity outside of the 8-km range in the redistribution process. In contrast, our observations show that absolute vorticity increased everywhere within 20 km from the center. In the idealized numerical experiments of Kloosterziel et al. (2007), inertially unstable barotropic anticyclones become stable within $T\sim 80/f$, or ~17 days at 21.2°N. Inertial instability may not have had sufficient time to develop in the anticyclone core. The vorticity decay could be attributed to other factors, such as interactions with surrounding vortices and the coast.

For baroclinic flows, the criterion for the so-called symmetric instability (e.g., Holton 1992, p. 279) is

$$fq<0, \tag{6}$$

where $q=(f+\zeta)N^2-\partial v/\partial z\,\partial B/\partial x$ is the Ertel potential vorticity, B the buoyancy and $N^2=\partial B/\partial z$ the buoyancy frequency. Using thermal wind balance, $\partial B/\partial x=f\partial v/\partial z$, one obtains $fq=f(f+\zeta)N^2-f^2(\partial v/\partial z)^2$. Baroclinicity has therefore a destabilizing effect owing to the contribution of the vertical shear $-f^2(\partial v/\partial z)^2$. This criterion is less stringent than the inertial instability criterion, and symmetric instability can develop even when the flow is inertially stable [$f(f+\zeta)>0$], provided that the vertical shear is sufficiently strong [$f^2(\partial v/\partial z)^2>f(f+\zeta)N^2$]. This mechanism is plausible since the flow was strongly baroclinic and $f+\zeta\approx 0$. However, the lack of observations of the vertical structure of the vortex precludes further quantification of this type of instability.

The criterion for the ageostrophic anticyclonic instability (AAI) (e.g., Molemaker et al. 2005) is

$$f(f+\zeta-\sigma)<0, \tag{7}$$

where $\sigma=[(\partial u/\partial x-\partial v/\partial y)^2+(\partial v/\partial x+\partial u/\partial y)^2]^{1/2}$ is the strain rate. The AAI criterion is also less stringent than the inertial instability criterion as it can act when $f+\zeta>0$. Figure 7 indicates that the AAI criterion was verified over a larger domain (Fig. 7b) encompassing the inertial instability domain (Fig. 7a). AAI is therefore another plausible mechanism to explain the rapid decay and broadening of the vortex and the appearance of smaller vortices in the anticyclone core after 1 November (Fig. 4). Again, the present observations are insufficient to detect the development of an AAI.

5. Frontal dynamics

The evolution of the SST, currents, vorticity, divergence, and strain fields are shown in Figs. 12, 13, and 14. On 23 October, the meridional front was at 158.46°W, near an area strained between cyclone L_1 and the developing vortex. By 25 October, the front had drifted to 158.61°W, following the translation of the vortex. A dipole of divergence formed across the front, the warm side being divergent and the cold side convergent. It was associated with $O(f)$ strain. A dipole of vorticity subsequently developed by 27 October, the warm side being anticyclonic and the cold side cyclonic, as a result of vortex stretching (cf. Fig. 11). By 29 October, the dipole of divergence had disappeared, and the dipole of vorticity, as well as strain, was weakening. These features are dynamically consistent with a meridional southward jet balancing the SST front, opposing the larger-scale northward flow between the vortex and cyclone L_1 farther west.

The 2D semigeostrophic (SG) frontal models of Hoskins and Bretherton (1972) and Davies and Müller (1988) may be used to further investigate frontal dynamics (they differ by their vertical structure). The 2D approximation, neglecting alongfront variations, is reasonable, given the small meridional standard deviations of SST and currents (Fig. 8). The SG approximation for strait fronts accounts for higher order corrections to the dynamics than the quasigeostrophic (QG) approximation (Snyder et al. 1991) and is therefore more appropriate for flows with large Ro. Both SG models capture the inviscid dynamics of a strait front on an f plane embedded in a large-scale deformation field

$$(U,V)=\left(-\frac{\overline{\sigma}}{2}x,\ \frac{\overline{\sigma}}{2}y\right),$$

where $\overline{\sigma}(t)$ is the depth-independent large-scale strain rate. The x axis is across front.

The SG models assume that the relative alongfront velocity $v'=v-V$ is in thermal wind balance (v and V are the subinertial local and large-scale velocities, respectively). In the presence of surface density gradients,

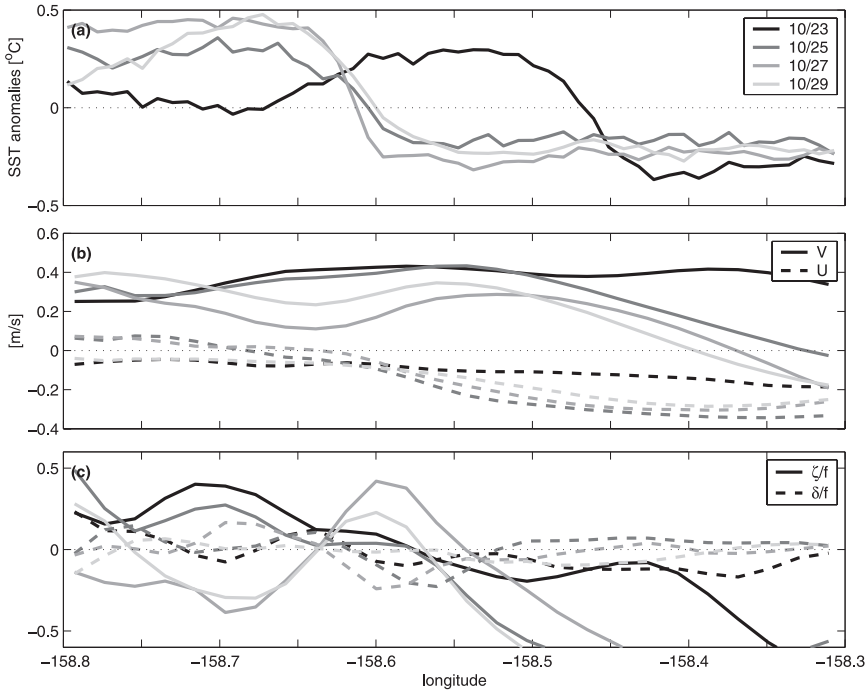

FIG. 13. Zonal sections, averaged over (21.1°–21.3°N), of (a) SST, (b) zonal (dashed) and meridional (solid) currents, and (c) vorticity (solid) and divergence (dashed) at the times shown in Fig. 12. The shading density decreases with time, as shown in the legend of (a).

straining by horizontal currents tends to destroy thermal wind balance, triggering an ageostrophic secondary circulation that maintains the balance (Hoskins and Draghici 1977; Hoskins et al. 1978). Expressed in geostrophic coordinates $(X, Z, T) = (x + v'/f, z, t)$, the vertical velocity is governed by the omega equation:

$$\frac{\partial^2 q w^*}{f \partial X^2} + f^2 \frac{\partial^2 w^*}{\partial Z^2} = \overline{\sigma} \frac{\partial^2 b}{\partial X^2}, \tag{8}$$

in which $q = fJ\partial b/\partial Z$ is the expression for the Ertel potential vorticity derived by Hoskins and Draghici (1977), b the buoyancy, $w^* = w/J, J = (1 - \zeta^*/f)^{-1}$ is the Jacobian of the coordinates transform, and $\zeta^* = \partial v'/\partial X$. The forcing term on the rhs of Eq. (8) is related to the vertical gradient of vorticity through thermal wind balance:

$$\frac{\partial^2 b}{\partial X^2} = f \frac{\partial \zeta^*}{\partial Z}. \tag{9}$$

Davies and Müller (1988) consider a semi-infinite layer $(-\infty < Z \leq 0)$ with uniform potential vorticity, yielding an exponentially decaying vertical structure for each horizontal Fourier component of v', with a decay scale inversely proportional to the wavenumber. With a rigid-lid surface, the solution expressed in physical space is

$$w = \frac{\overline{\sigma}}{2f} z\zeta. \tag{10}$$

Surface divergence $\delta_0 = (-\partial w/\partial z)_{z=0}$ is then proportional to surface vorticity ζ_0:

$$\delta_0 = -\frac{\overline{\sigma}}{2f}\zeta_0. \tag{11}$$

Hoskins and Bretherton (1972) consider a finite depth layer $(-H \leq z \leq 0)$ with zero potential vorticity, yielding a linearly decaying vertical structure for v'. Mass conservation constrains the alongfront velocity to be opposite at the bottom and at the surface: $v'(-H) = -v'(0)$. With a rigid-lid surface, the solution is

$$w = \frac{\overline{\sigma}}{f} Z \left(\frac{Z}{H} + 1\right) J \left.\frac{\partial v'}{\partial X}\right|_{Z=0}. \tag{12}$$

Surface divergence is then also proportional to surface vorticity, but with twice the coefficient of Eq. (11):

$$\delta_0 = -\frac{\overline{\sigma}}{f}\zeta_0. \tag{13}$$

To check which of these idealized models is consistent with the observations, the large-scale strain rate $\overline{\sigma}$, the

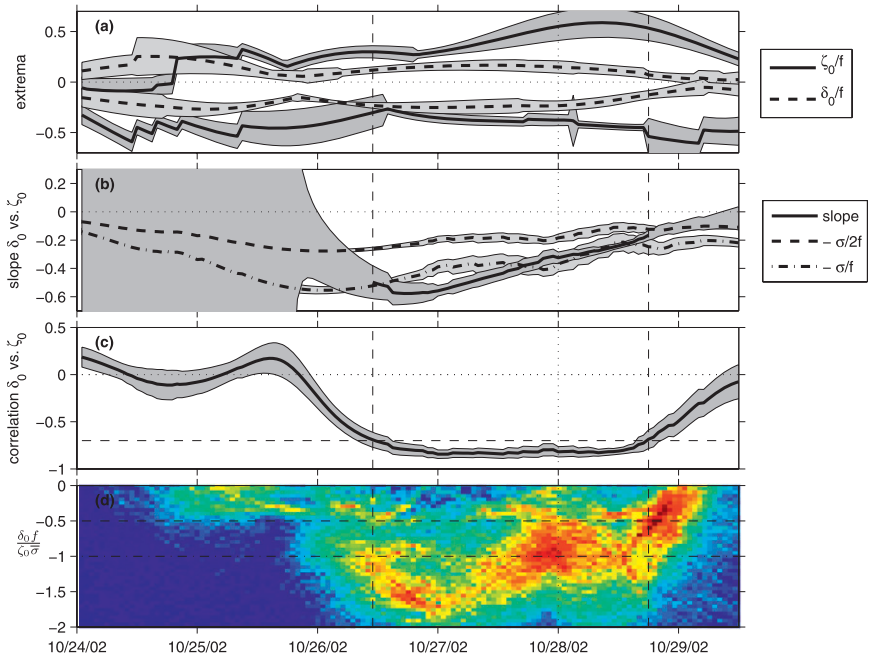

FIG. 14. (a) Extrema of vorticity (solid) and divergence (dashed) over the region of the front, (b) slope of the principal axis of covariance of surface divergence and vorticity (solid), (c) associated correlation coefficient, and (d) temporal evolution of the distribution of $\kappa = \delta_0 f/\zeta_0\overline{\sigma}$ for all grid points in the different areas used to estimate $\overline{\sigma}$ [the numbers of occurrences of κ values are given by the color scale, where red (blue) represents higher (lower) numbers, with an arbitrary normalization]. The predictions from the semigeostrophic models of Hoskins and Bretherton (1972) (dashed–dotted) and Davies and Müller (1988) (dashed) are indicated in (b) and (d). Shading indicates uncertainties.

correlation coefficient between surface divergence and vorticity, the slope of the covariance ellipses (Fig. 15), and the nondimensional number

$$\kappa = \frac{\delta_0 f}{\zeta_0 \overline{\sigma}} \tag{14}$$

were estimated over a domain straddling the SST front. Here $\overline{\sigma}$ was estimated by least squares fit, constraining the large-scale currents to be nondivergent. Uncertainties were obtained by varying the size and position of the estimation domain (black rectangles in Fig. 12). The domain was restricted to 21.1°–21.3°N where the front remained meridional. The domain was initially centered on the SST front and then incrementally shifted westward until its eastern boundary was 4 km east of the front to capture the frontal asymmetry. For each position, the width of the domain was varied from 10 to 30 km. The mean and standard deviation of the quantities computed over these various domains are shown in Fig. 14.

At the beginning of 26 October the large-scale strain rate $\overline{\sigma}$ reached an extremum of $\sim 0.6f$ (Fig. 14b). This was large enough to trigger frontogenesis, which lasted 3 days (26–29 October), as suggested by the significant negative values of the correlation coefficient ($r < -0.7$, Fig. 14c). The slope of the covariance ellipses of δ_0 and ζ_0 over the front reached an extremum value of approximately -0.6 by the end of 26 October and diminished afterward, paralleling the evolution of $\overline{\sigma}$ (Fig. 14b). To further document the frontogenesis process, the temporal evolution of the distribution of κ is also shown in Fig. 14d.

During the active phase of frontogenesis, centered on 28 October, the prediction of Hoskins and Bretherton (1972), $\delta_0/\zeta_0 = -\overline{\sigma}/f$ or $\kappa = -1$, was more representative of the observations than the prediction of Davies and Müller (1988), $\delta_0/\zeta_0 = -\overline{\sigma}/2f$ or $\kappa = -½$. This suggests that the front was confined to the surface mixed layer (zero potential vorticity) and that v' was of opposite signs at the base of the mixed layer and at the surface. A band of anticyclonic vorticity at the bottom of the mixed layer thus would have formed east of the front, which our surface observations cannot confirm.

The extremum values of vorticity and divergence over the front are shown in Fig. 14a. The front became asymmetric during the active phase of frontogenesis, with

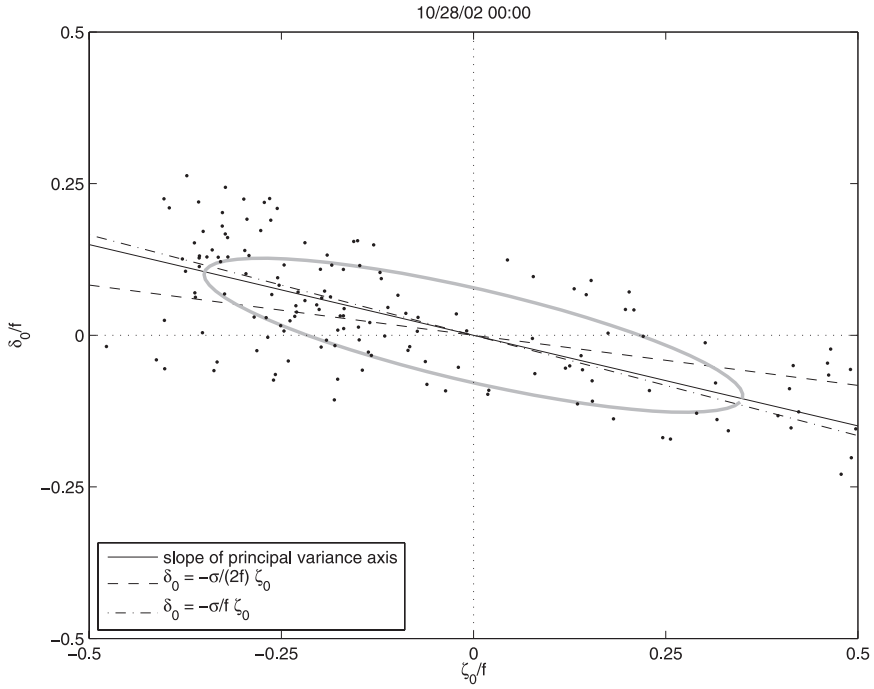

FIG. 15. Scatterplot of divergence (y axis) vs vorticity (x axis) over a rectangular area between 21.1° and 21.3°N spanning 30 km zonally across the front on 28 Oct 2002. The average vorticity and divergence over the area were removed. The gray ellipse represents the covariance matrix eigenvalues and eigenvectors. The solid line shows the slope of the principal axis. The slopes predicted from the semi-infinite (dashed) and the mixed layer (dashed–dotted) frontal models are also indicated.

cyclonic vorticity and convergence stronger on the cold side of the front (reaching $0.59f$ and $-0.25f$) and anticyclonic vorticity and divergence weaker on the warm side of the front (reaching $-0.45f$ and $0.17f$). This asymmetry is in agreement with SG dynamics and not with QG dynamics, which would yield vorticity symmetry. Indeed, the vortex stretching term in Eq. (3) is proportional to the absolute vorticity $f + \zeta$ (instead of f for QG dynamics) and is therefore stronger for cyclonic than for anticyclonic vorticity (Fig. 11, second column), given similar magnitudes of divergence. This results in faster cyclonic vorticity growth (Fig. 11, first column). Because surface divergence is proportional to surface vorticity, following Eq. (13), convergence becomes stronger than divergence (Fig. 12, third column, and Fig. 14a), further enhancing the vortex stretching term responsible for cyclonic vorticity growth, in a positive feedback loop.

6. Summary and discussion

High-resolution observations reveal energetic ageostrophic submesoscale structures embedded in a field of mesoscale eddies in the lee of the Hawaiian Islands. A strong anticyclonic vortex of ~15 km radius formed inside an anticyclonic meander associated with two larger cyclones west and south of Oahu. Local vorticity grew from $-f$ to $-1.7f$ in 4 days, possibly driven by negative wind stress curl in the lee of Oahu. The flow was ageostrophic near the center and around the periphery of the vortex. Absolute vorticity remained negative for 9 days. The vortex was prone to inertial, symmetric, and anticyclonic ageostrophic instabilities, but the temporal evolution of radial profiles of vorticity was inconsistent with angular momentum redistribution by inertial instability.

A sharp SST front developed between the vortex and cyclone L_1 to the west due to the large-scale horizontal strain rate $\overline{\sigma}$. An ageostrophic circulation maintained thermal wind balance between alongfront vertical shear and cross-front density gradient and lasted for ~3 days, as revealed by anticorrelated surface divergence and vorticity. Their ratio was consistent with a semigeostrophic model of a front confined to the surface mixed layer, which predicts $-\overline{\sigma}/f$. Models of fronts decaying exponentially in an infinitely deep ocean (Davies and Müller 1988; Lapeyre and Klein 2006b) predict only half of the observed ratio.

The wind effects on the dynamics of the front were neglected in section 5. The Ekman transport is generally modulated by mesoscale vorticity, resulting in a dipole of Ekman convergence and divergence along a jet parallel to the wind (Niiler 1969; Stern 1975). This mechanism was invoked by Flament et al. (1985) and Flament and Armi (2000) to explain cyclonic frontogenesis along upwelling jets in the California Current. More recently, Thomas and Lee (2005) showed that downfront winds drive a frontogenetic ageostrophic circulation due to cross-frontal advection of buoyancy and vorticity by the Ekman flow. Here, the trade winds were blowing at $\sim$10 m s^{-1} (Fig. 5c) with a downfront component during 26–29 October and therefore may have reinforced the front. However, the tight correlation between divergence and vorticity (Fig. 14c), consistent with the prediction of Eq. (13), suggests that strain-driven frontogenesis dominated.

Submesoscale processes appear widespread, even in the open ocean. Munk et al. (2000) documented the ubiquitous presence of cyclonic submesoscale eddies in sun glitter and synthetic aperture radar images from space. In the North Pacific Flament and Armi (2000), using clusters of mixed layer drifters, and Rudnick (2001), using shipboard acoustic Doppler current profiler (ADCP) observations, have reported a significant skewness toward cyclonic vorticity, with the largest values occurring at scales less than a few kilometers. Munk et al. (2000) proposed that submesoscale cyclonic eddies are generated by instabilities of surface density fronts strained by mesoscale confluence, which develop faster on the cyclonic than on the anticyclonic side of fronts owing to the asymmetry of the vortex stretching term in the vorticity equation (3). They argue that cyclonic vorticity can reach values stronger than f, whereas anticyclonic vorticity is limited by $-f$ due to inertial instabilities. However, the present observations show that anticyclonic vorticity below $-f$ may form and persist for several days before inertial instability may have time to develop. Subinertial vorticities of approximately $-2f$ have also been observed along the coast of the Florida Keys by Shay et al. (1998).

Coherent submesoscale structures associated with large vorticity, divergence, and strain, such as observed here, are pervasive in high-resolution O(1 km) numerical simulations (Mahadevan and Tandon 2006; Capet et al. 2008a,b; Klein et al. 2008). These studies suggest that submesoscale structures have a significant impact on the larger-scale ocean circulation, air–sea interactions, and biochemical processes (see the review by Thomas et al. 2008). Parameterizations of submesoscale motions (e.g., Fox-Kemper et al. 2008; Fox-Kemper and Ferrari 2008) need to be developed and tested against observations, such as those presented here.

Acknowledgments. Section 5 owes its existence to vivid discussion with P. Klein on frontogenesis in the upper ocean. Fruitful interactions with G. Carter, E. Firing, R. Kloosterziel, D. Luther, M. Merrifield, and L. Thomas are gratefully acknowledged. Constructive comments and suggestions from two anonymous reviewers significantly contributed to improve the manuscript. The HFRs and ADCP moorings were deployed and the data were processed with the help of O. Ali, F. Ascani, J. Aucan, C. Bandet, M. Bandet, J. Benito, M. Bour, T. Decloedt, J. Degoulet, S. Delambert, J. Deshayes, A. Desoria, B. Dousset, P. Dutrieux, T. Dutrieux, Y. Firing, I. Flament, M. Flament, M. Hamann, T. Helzel, M. Kniephoff, O. Koshe, K. Millikan, P. Moravcik, M. Pinkerton, and D. Young. Permits were obtained with the assistance of J. Morgan and K. Williams (Ko Olina Resort Association); K. Breaux, L. Hayashi, and R. Shigemura (U.S. Air Force Kaena Point Satellite Tracking Station); and M. Alkire, A. Jodar, and P. Miyashiro (Hawaii State Department of Land and Natural Resources). The HFR processing routines by J. Paduan and M. Cook were adapted to compute the vector currents from the radial measurements. The altimeter data were produced by SSALTO/DUACS/AVISO, and the SST and ocean color images were produced by the NASA Goddard Space Flight Center. The construction of the HFRs was supported by NSF Major Research Instrumentation Grant OCE-9724464, and their deployment by NSF Grants OCE-9819534 and OCE-0453848 (HOME) to P. F.; additional support to C. C. was provided by NSF Grant OCE-0426112. This publication uses CTD data from the Hawaii Ocean Time Series, supported by NSF Grant OCE-0327513, and ADCP data from the C1 mooring deployed by D. Luther, supported by NSF Grant OCE-9819533 (HOME). This paper was prepared under Cooperative Agreement NA07NOS4730207 from the NOAA/IOOS Program Office, U.S. Department of Commerce.

APPENDIX

Instruments and Datasets

Two 16-MHz high-frequency radio Doppler current meters were deployed along the west shore of Oahu (Fig. 1b) from September 2002 to May 2003. Each HFR measured the radial component of surface currents in the direction of the instrument at 1.2-km radial resolution and 7°–15° azimuthal resolution, averaged over 9 min every 20 min. Radial currents were hourly averaged, and vector currents were mapped on a 2-km resolution Cartesian grid by least squares fitting the zonal and meridional components to the hourly radial observations in a 2-km search radius (see appendix A in Chavanne et al.

2007). The range of useful data was limited by geometric dilution of precision (GDOP).

The 300- and 75-kHz acoustic Doppler current profilers (ADCPs) were moored upward looking at 90 m and 750 m below the surface in 4700-m water depth (labeled C1 in Fig. 1b), with vertical resolutions of 4 and 8 m, and 10-min acquisitions. Correlations between the 12-m-depth bin of the upper ADCP and the nearest HFR grid cell were 0.9 for the radial and zonal components but dropped to 0.5 for the meridional component (still significant to 95% confidence), illustrating the GDOP of the HFR data.

The 33-km-resolution gridded geostrophic altimetric currents (Ducet et al. 2000) were used to provide the broader context for the HFR observations. They were produced by Segment Sol Multimissions d'Altimétrie, d'Orbitographie et de Localisation Précise/Data Unification and Altimeter Combination System (SSALTO/DUACS) and distributed by Archiving, Validation, and Interpretation of Satellite Oceanographic data (AVISO; available online at http://www.aviso.oceanobs.com/). Wind stress at 25-km resolution was obtained from QuikSCAT (Liu and Tang 1996), complemented by observations of the 10-m wind at Honolulu International Airport. The 1-km resolution sea surface temperature (SST) and chlorophyll-*a* concentrations were obtained from the Moderate Resolution Imaging Spectroradiometer (MODIS) on board *Aqua* and *Terra* (level 2 data products). Nighttime SST images (to avoid island wake diurnal warming, e.g., Barton et al. 2000) less than one inertial period apart were combined to reduce loss of coverage from clouds.

REFERENCES

Barton, E. D., G. Basterretxea, P. Flament, E. G. Mitchelson-Jacob, B. Jones, J. Aristegui, and F. Herrera, 2000: Lee region of Gran Canaria. *J. Geophys. Res.,* **105,** 17 173–17 193.

Blumen, W., 1978: Uniform potential vorticity flow: Part I. Theory of wave interactions and two-dimensional turbulence. *J. Atmos. Sci.,* **35,** 774–783.

Capet, X., J. C. McWilliams, M. J. Molemaker, and A. F. Shchepetkin, 2008a: Mesoscale to submesoscale transition in the California Current system. Part I: Flow structure, eddy flux, and observational tests. *J. Phys. Oceanogr.,* **38,** 29–43.

——, ——, ——, and ——, 2008b: Mesoscale to submesoscale transition in the California Current system. Part II: Frontal processes. *J. Phys. Oceanogr.,* **38,** 44–64.

Chavanne, C., P. Flament, R. Lumpkin, B. Dousset, and A. Bentamy, 2002: Scatterometer observations of wind variations induced by oceanic islands: Implications for wind-driven ocean circulation. *Can. J. Remote Sens.,* **28,** 466–474.

——, I. Janeković, P. Flament, P.-M. Poulain, M. Kuzmić, and K.-W. Gurgel, 2007: Tidal currents in the northwestern Adriatic: High-frequency radio observations and numerical model predictions. *J. Geophys. Res.,* **112,** C03S21, doi:10.1029/2006JC003523.

——, P. Flament, G. Carter, M. Merrifield, D. Luther, E. Zaron, and K.-W. Gurgel, 2010a: The surface expression of semidiurnal internal tides near a strong source at Hawaii. Part I: Observations and numerical predictions. *J. Phys. Oceanogr.,* **40,** 1155–1179.

——, ——, D. Luther, and K.-W. Gurgel, 2010b: The surface expression of semidiurnal internal tides near a strong source at Hawaii. Part II: Interactions with mesoscale currents. *J. Phys. Oceanogr.,* **40,** 1180–1200.

Davies, H. C., and J. C. Müller, 1988: Detailed description of deformation-induced semi-geostrophic frontogenesis. *Quart. J. Roy. Meteor. Soc.,* **114,** 1201–1219.

Ducet, N., P. Y. Le Traon, and G. Reverdin, 2000: Global high-resolution mapping of ocean circulation from TOPEX/Poseidon and ERS-1 and -2. *J. Geophys. Res.,* **105** (C8), 19 477–19 498.

Flament, P., and L. Armi, 2000: The shear, convergence, and thermohaline structure of a front. *J. Phys. Oceanogr.,* **30,** 51–66.

——, ——, and L. Washburn, 1985: The evolving structure of an upwelling filament. *J. Geophys. Res.,* **90** (C6), 11 765–11 778.

——, R. Lumpkin, J. Tournadre, and L. Armi, 2001: Vortex pairing in an unstable anticyclonic shear flow: Discrete subharmonics of one pendulum day. *J. Fluid Mech.,* **440,** 401–409.

Fox-Kemper, B., and R. Ferrari, 2008: Parameterization of mixed layer eddies. Part II: Prognosis and impact. *J. Phys. Oceanogr.,* **38,** 1166–1179.

——, ——, and R. Hallberg, 2008: Parameterization of mixed layer eddies. Part I: Theory and diagnosis. *J. Phys. Oceanogr.,* **38,** 1145–1165.

Fujieki, L., F. Santiago-Mandujano, C. Hannides, R. Lukas, and D. Karl, 2005: Hawaii Ocean Time-series Program data report 14, 2002. University of Hawaii at Manoa School of Ocean and Earth Science and Technology 279 pp.

Held, I. M., R. T. Pierrehumbert, S. T. Garner, and K. L. Swanson, 1995: Surface quasi-geostrophic dynamics. *J. Fluid Mech.,* **282,** 1–20.

Holton, J. R., 1992: *An Introduction to Dynamic Meteorology*. 3rd ed. Academic Press, 511 pp.

Hosegood, P., M. C. Gregg, and M. H. Alford, 2008: Restratification of the surface mixed layer with submesoscale lateral density gradients: Diagnosing the importance of the horizontal dimension. *J. Phys. Oceanogr.,* **38,** 2438–2460.

Hoskins, B. J., and F. P. Bretherton, 1972: Atmospheric frontogenesis models: Mathematical formulation and solution. *J. Atmos. Sci.,* **29,** 11–37.

——, and I. Draghici, 1977: The forcing of ageostrophic motion according to the semi-geostrophic equations and in an isentropic coordinate model. *J. Atmos. Sci.,* **34,** 1859–1867.

——, ——, and H. C. Davies, 1978: A new look at the ω-equation. *Quart. J. Roy. Meteor. Soc.,* **104,** 31–38.

Klein, P., B. L. Hua, G. Lapeyre, X. Capet, S. Le Gentil, and H. Sasaki, 2008: Upper ocean turbulence from high-resolution 3D simulations. *J. Phys. Oceanogr.,* **38,** 1748–1763.

Kloosterziel, R. C., G. F. Carnevale, and P. Orlandi, 2007: Inertial instability in rotating and stratified fluids: Barotropic vortices. *J. Fluid Mech.,* **583,** 379–412.

Kunze, E., 1985: Near-inertial wave propagation in geostrophic shear. *J. Phys. Oceanogr.,* **15,** 544–565.

Lapeyre, G., and P. Klein, 2006a: Dynamics of the upper oceanic layers in terms of surface quasigeostrophy theory. *J. Phys. Oceanogr.,* **36,** 165–176.

——, and ——, 2006b: Impact of the small-scale elongated filaments on the oceanic vertical pump. *J. Mar. Res.,* **64,** 835–851.

Liu, W. T., and W. Tang, 1996: Equivalent neutral wind. Jet Propulsion Laboratory Publ. 96-17, 16 pp.

Lumpkin, R., 1998: Eddies and currents of the Hawaiian Islands. Ph.D. thesis, University of Hawaii at Manoa, 281 pp.

Luther, D. S., 1985: Trapped waves around the Hawaiian Islands. *Hawaiian Ocean Experiment: Proc. 3rd 'Aha Huliko'a Hawaiian Winter Workshop,* Honolulu, HI, University of Hawaii at Manoa, 261–301.

Mahadevan, A., and A. Tandon, 2006: An analysis of mechanisms for submesoscale vertical motion at ocean fronts. *Ocean Modell.,* **14,** 241–256.

Merrifield, M. A., L. Yang, and D. S. Luther, 2002: Numerical simulations of a storm-generated island-trapped wave event at the Hawaiian Islands. *J. Geophys. Res.,* **107,** 3169, doi:10.1029/2001JC001134.

Molemaker, M. J., J. C. McWilliams, and I. Yavneh, 2005: Baroclinic instability and loss of balance. *J. Phys. Oceanogr.,* **35,** 1505–1517.

Munk, W., L. Armi, K. Fischer, and F. Zachariasen, 2000: Spirals on the sea. *Proc. Roy. Soc. London,* **456,** 1217–1280.

Niiler, P. P., 1969: On the Ekman divergence in an oceanic jet. *J. Geophys. Res.,* **74,** 7048–7052.

Patzert, W. C., 1969: Eddies in Hawaiian waters. University of Hawaii at Manoa Hawaiian Institute of Geophysics Tech. Rep. 69-8, 51 pp.

Roden, G. I., 1981: Mesoscale thermohaline, sound velocity and baroclinic flow structure of the Pacific Subtropical Front during the winter of 1980. *J. Phys. Oceanogr.,* **11,** 658–675.

Rudnick, D. L., 2001: On the skewness of vorticity in the upper ocean. *Geophys. Res. Lett.,* **28,** 2045–2048.

Shay, L. K., T. N. Lee, E. J. Williams, H. C. Graber, and C. G. H. Rooth, 1998: Effects of low-frequency current variability on near-inertial submesoscale vortices. *J. Geophys. Res.,* **103** (C9), 18 691–18 714.

Snyder, C., W. C. Skamarock, and R. Rotunno, 1991: A comparison of primitive-equation and semigeostrophic simulations of baroclinic waves. *J. Atmos. Sci.,* **48,** 2179–2194.

Stern, M. E., 1975: *Ocean Circulation Physics*. International Geophysical Series, Vol. 19, Academic Press, 246 pp.

Thomas, L. N., and C. M. Lee, 2005: Intensification of ocean fronts by down-front winds. *J. Phys. Oceanogr.,* **35,** 1086–1102.

——, A. Tandon, and A. Mahadevan, 2008: Submesoscale processes and dynamics. *Ocean Modeling in an Eddying Regime, Geophys. Monogr.,* Vol. 177, Amer. Geophys. Union, 17–38.